SAND2022-14109C

A Method to Expand Sparse Set Acceleration Data to Full Set Strain Data

Jonathan Hower[1], Raymond Joshua[1], Tyler Schoenherr[2]

[1]Honeywell Federal Manufacturing & Technologies*
14520 Botts Rd
Kansas City, MO, 64147

[2]Sandia National Laboratories**
PO Box5800 - MS0557
Albuquerque, NM, 87185

Abstract

Expansion methods are commonly used to compute the response at locations not measured during physical testing. The System Equivalent Reduction Expansion Process (SEREP) produces responses at finite element degrees of freedom through the mode shapes of that model. Measurements used for expansion are often acceleration, strain, and displacement and operate only on like sets of data. For example, expanding acceleration data produces only additional acceleration data and does not provide insight into the test article's stress or strain state. Stress and strain are often desired to evaluate yield limits and create fatigue models. The engineer may have acceleration measurements available, but desire a component's stress and strain state. This work evaluates a physical experiment from which acceleration is measured and a full set of strain, stress and displacement data is obtained through SEREP and integration.

Honeywell Federal Manufacturing & Technologies, LLC operates the Kansas City National Security Campus for the United States Department of Energy / National Nuclear Security Administration under Contract Number DE-NA0002839

Keywords
SEREP, Expansion, Acceleration, Strain

1 Introduction

System Equivalent Reduction Expansion Process (SEREP) was initially developed by O'Callahan [1] as a global mapping technique to estimate rotational degrees of freedom (DOFs) for experimental modal data. Since inception, it has been used for multiple applications. One early application of the process involved model reduction to reduce large analytical models when performing correlation studies between a model and physical experiment. Recent applications of SEREP involve expanding a sparse set of measurements from a physical test to a full set by the mode shapes of a finite element model [2, 3]. The goal of this effort is to compute the stress and strain state of a component under dynamic loads using only acceleration measurements and a finite element model. Although this method is valid for both stress and strain, only strain results are presented because there are no means to directly measure stress state.

A simple physical test structure was created, known as the bobble head, and represents a cantilever beam with a mass at the tip. The structure was placed on an electrodynamic shaker and subjected to a multi-axis random vibration load. A set of accelerometers were placed about the structure to measure response and are used for strain computation. A set of strain gauges were placed about the structure for validation of the proposed strain estimation method. These measured strains were not used in the strain estimation process.

An uncalibrated finite element model was created and all modes in the frequency band of interest were computed. The acceleration measurements were expanded through SEREP with the finite element mode shapes and compared to the measured data for verification. Displacements were estimated by integrating and filtering the measured accelerations. These estimated displacements were then expanded through SEREP. The expanded displacement data was then converted to strain data by performing a linear transformation through the finite element model. Finally the expanded strains were compared to the strains measured during the physical test.

2 Background Theory

2.1 Expansion Method

This paper applies SEREP as introduced by O'Callahan [1]. In literature, SEREP has been performed on accelerations, displacements and strains [2, 3, 4]. The equation for SEREP is shown as Eq. 1 and is performed by expanding a sparse set, $\bar{x}_a$, to a full set, $\bar{x}_n$ by performing a linear transformation through the transformation matrix, T. The transformation matrix is a function of the full, ϕ_n, and sparse, ϕ_a, mode shape matrices as shown in Eq. 2. The superscript ^{g} indicates the generalized inverse and is shown in Eq. 3.

$$\bar{x}_n(t) = T\bar{x}_a(t) \tag{1}$$

$$T = \phi_n {\phi_a}^g \tag{2}$$

$$\phi^g = (\phi^\top \phi)^{-1}\phi^\top \tag{3}$$

2.2 Estimating Displacement from Acceleration

Displacement was estimated from accelerometer data by integration and bandpass filtering. Acceleration data was integrated twice via cumulative trapezoidal numerical integration. Prior to integration, data was filtered with a fifth order Butterworth bandpass filter. The proposed approach is displayed visually in Fig. 1. It is thought that filtering out low frequency response reduced the affect of drift when double integrating and filtering out high frequency response reduced integration errors due to high frequency noise in the signal. The bandpass frequencies were set to 50 and 2,000 Hz. Multiple techniques exists in literature to estimate displacement from acceleration. The proposed technique is a simple approach to estimate displacement when compared to other methods [5, 6]. No displacement measurements were taken, so the accuracy of the proposed approach cannot be directly validated. Instead, the estimate is verified by a differentiating process as described in Section 2.4.2.

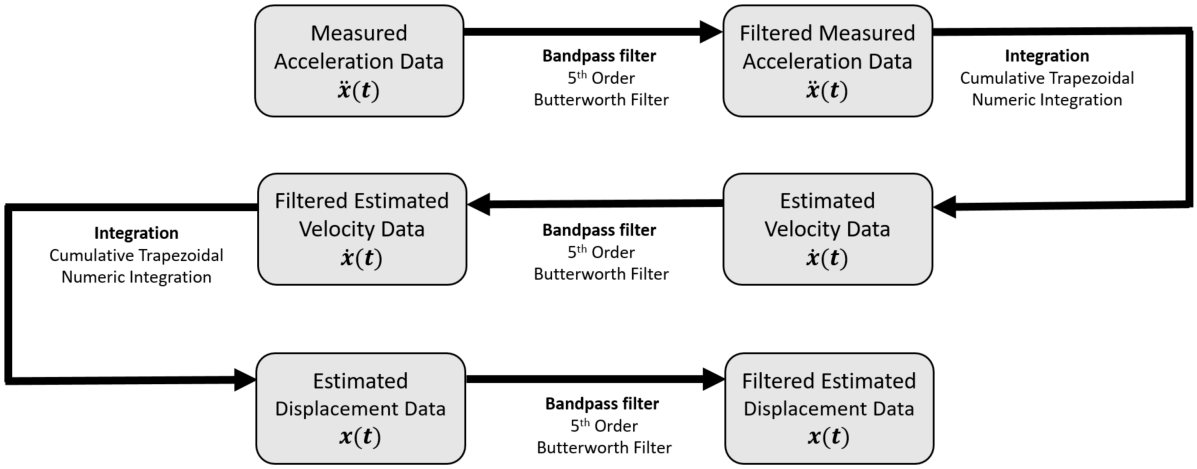

Figure 1: Method to estimate displacement from acceleration.

2.3 Transformation of Displacement to Stress & Strain

Generally, a set of DOF responses at a point in time, $\overline{\alpha}(t)$, may be written as a function of its mode shape matrix, ϕ, and a modal weighting vector, $\overline{P}(t)$ shown as Eq. 4.

$$\overline{\alpha}(t) = \phi \overline{P}(t) \tag{4}$$

Particularly, these DOFs may be defined as displacement, strain and stress vectors shown in Eq. 5, 6, & 7 respectively.

$$\overline{x}(t) = \phi \overline{P}(t), \tag{5}$$

where $\overline{x}(t)$ is the displacement vector at time, t, ϕ is the displacement mode shape matrix and $\overline{P}(t)$ is the modal weighting vector at time, t.

$$\overline{\varepsilon}(t) = \phi_{\varepsilon} \overline{P}(t) \tag{6}$$

where $\overline{\varepsilon}(t)$ is the strain vector at time, t, ϕ_{ε} is the strain mode shape matrix and $\overline{P}(t)$ is the modal weighting vector at time, t.

$$\overline{\sigma}(t) = \phi_{\sigma} \overline{P}(t) \tag{7}$$

where $\overline{\sigma}(t)$ is the stress vector at time, t, ϕ_{σ} is the stress mode shape matrix and $\overline{P}(t)$ is the modal weighting vector at time, t.

For displacements, strains and stresses, it holds true that the modal weighting vector, $\overline{P}(t)$, is constant. Therefore Eq. 6 & 7 may be written in terms of the displacement vector, the displacement mode shape matrix and their respective mode shape matrices. Solving for the strain vector yields Eq. 8 and solving for the stress vector yields Eq. 9.

$$\overline{\varepsilon}(t) = \phi_{\varepsilon} \phi^{g} \overline{x}(t) \tag{8}$$

$$\overline{\sigma}(t) = \phi_{\sigma} \phi^{g} \overline{x}(t) \tag{9}$$

2.4 Verification Metrics

2.4.1 Modal Projection Error

The modal projection error (MPE), introduced by Schoenherr [7], provides insight on how well one set of mode shapes can be projected onto another set of mode shapes. For this research, it will indicate the model's ability to represent the measured data at some instance in time. For example, if a linear combination of the mode shapes computed from the finite element model can properly represent the measured response at an instance in time, the MPE will be low. The equation for MPE as derived by Schoenherr [8] is shown as Eq. 10.

$$MPE(t) = 1 - \overline{X}_a(t)^g \phi_a \phi_a{}^g \overline{X}_a(t) \tag{10}$$

2.4.2 Double Differentiation

The estimated displacements cannot be directly compared to the physical displacements because there was no direct displacement measurement of the test hardware under load. In order to verify the displacement estimation, the estimated displacements over time were differentiated twice to compute a reconstructed acceleration. This reconstructed acceleration was then compared to the measured acceleration. The workflow of this process is shown in Fig. 2.

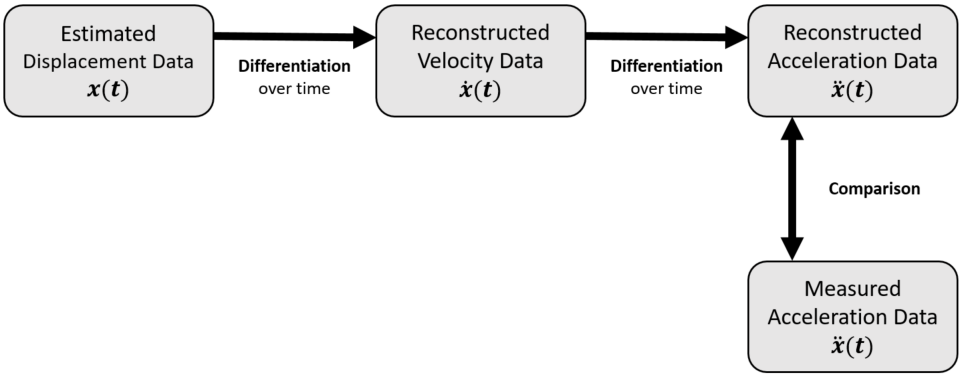

Figure 2: Method to verify estimated displacements from reconstructed acceleration.

2.5 Error Metrics

Multiple error metrics were used to evaluate the efficacy of the acceleration expansion and strain estimation methods. The values $\overline{X}$ may represent acceleration or strain data. The subscript $_{meas}$ represents data that has been physically measured while $_{pred}$ represents data that was predicted through analysis. The subscripts $_t$ and $_f$ represent time domain and frequency domain data respectively. The number of values in the time and frequency domain data sets are represented by n_t & n_f respectively. For all frequency domain error metrics, the power spectral density (PSD) values were used. PSD's were computed via Welch's method with a 50% overlap, a Hamming window and a total of seven averages. Supplementary error metrics are introduced in Appendix A.3.

2.5.1 Root Mean Square

The root mean square (RMS) values are used as error metrics and computed in both the time and frequency domain. The time domain RMS value is computed by Eq. 11 below. The frequency domain RMS, often called g_{RMS} for acceleration data, is the square root of the area under the PSD vs. frequency curve and was computed per Irvine [9].

$$RMS_{time} = \sqrt{\frac{1}{n_t}\sum_t |\overline{X}_t|^2} \tag{11}$$

2.5.2 Mean Absolute Error

The mean absolute error (MAE) compares two signals by averaging the absolute values of the data set. It may be computed in the time or frequency domain, as shown in Eq. 12 & 13 respectively. A low MAE indicates good agreement between measured and predicted values.

$$MAE_{time} = \frac{1}{n_t} \sum_{t} |\overline{X}_{t,meas} - \overline{X}_{t,pred}| \tag{12}$$

$$MAE_{freq} = \frac{1}{n_f} \sum_{f} |\overline{X}_{f,meas} - \overline{X}_{f,pred}| \tag{13}$$

3 Proposed Method

The goal of this paper is to define and evaluate a process to compute full set stress and strain data from sparse accelerometer measurements. As stated, this paper focuses on strain data because stress cannot be measured physically. The steps in the process are described below and visually displayed in Fig. 3.

The bobble head was subjected to random vibration loading. On the structure, a sparse set of acceleration data was collected for strain estimation and a sparse set of strain data was collected for validation. Next, sparse displacements were estimated through integration and filtering as described in Section 2.2. The sparse displacements were then expanded through SEREP, Eq. 1, and converted to strains through a linear transformation, Eq. 8. Displacement and strain mode shape matrices were computed from a finite element model. The estimated strains were then compared to measured strains at sparse locations as described in Section 2.5. Additionally, sparse accelerations were expanded and compared in the same manner as described above. Acceleration expansion was performed to verify the expansion process prior to strain estimation.

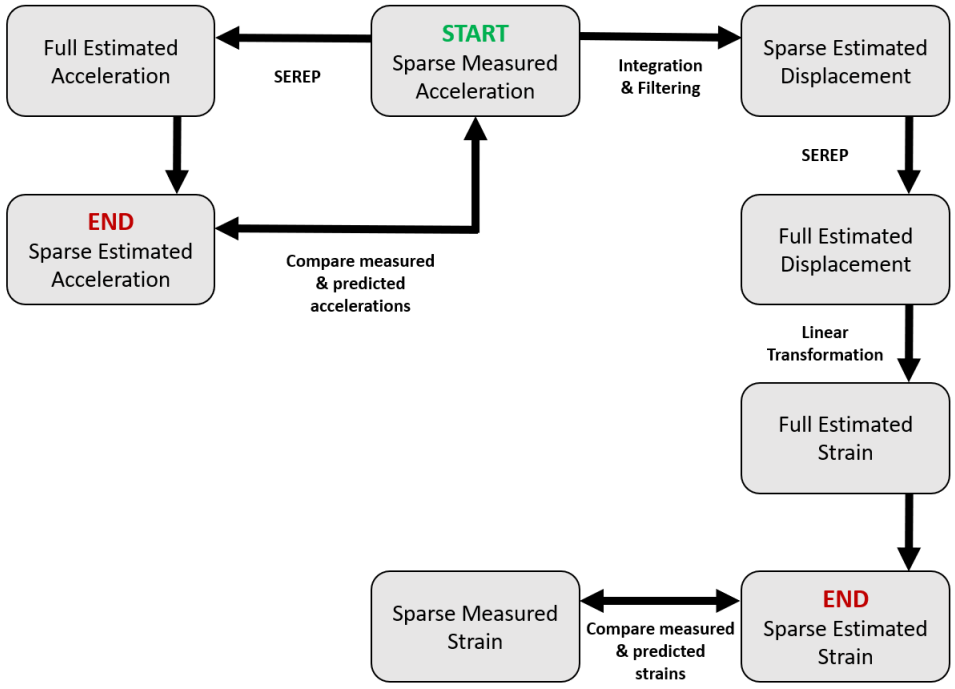

Figure 3: Workflow for acceleration expansion and full set strain estimation from sparse set acceleration data.

There are a few limitations of this approach worth noting. First, the strain estimate is sensitive to the filter frequencies because it suffered from significant drift in the displacement estimation when the the high-pass filter was not used. This error is created

when estimating displacements and is carried through the entire process ultimately affecting the strain estimate. Second, the accuracy of the displacement estimate is not known because there was no direct measurement of displacement on the physical structure under load. Last, the accuracy of the finite element mode shapes used for expansion and strain estimation is not known because experimental modal analysis on the physical test structure was not performed.

4 Physical Test Hardware and Environment

The the bobble head represents a cantilever beam with a large mass at the tip. The structure is comprised of a base plate $(6" \times 6" \times 0.375")$, beam $(0.375" \times 0.5" \times 3.125")$ and block $(2" \times 2" \times 2")$. All components are made from aluminum and are mechanically fastened via bolts. For this test, the bobble head was mounted to an electrodynamic shaker as shown in Figure 4.

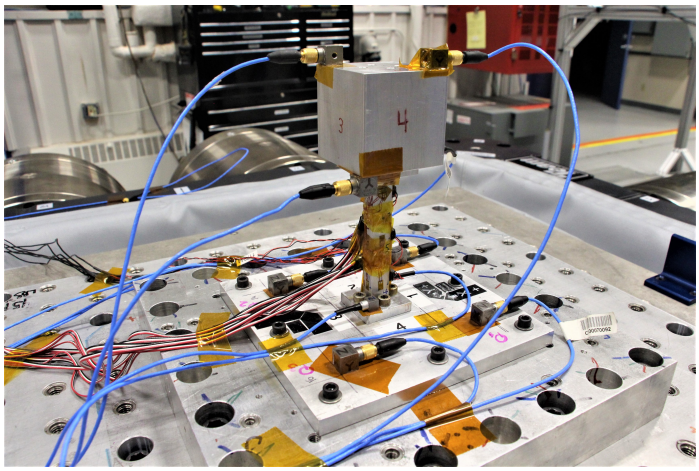

Figure 4: Instrumented bobble head test structure mounted atop electrodynamic shaker.

The bobble head was subjected to a multi-axis random vibration loading. The test profile had a target of 3 g_{rms} for all axes and was controlled to 2 kHz. All data was filtered via a 5^{th} order Butterworth filter with bandpass frequencies of 50 and 2,000 Hz. The bobble head was instrumented with ten triaxial accelerometers distributed about the base plate and block and six uniaxial accelerometers distributed about the beam. Five strain gauges and one strain rosette were distributed along the beam. One of the strain gauges recorded poor data and was not used for this analysis. The locations of all instrumentation used for analysis are show in Figure 5.

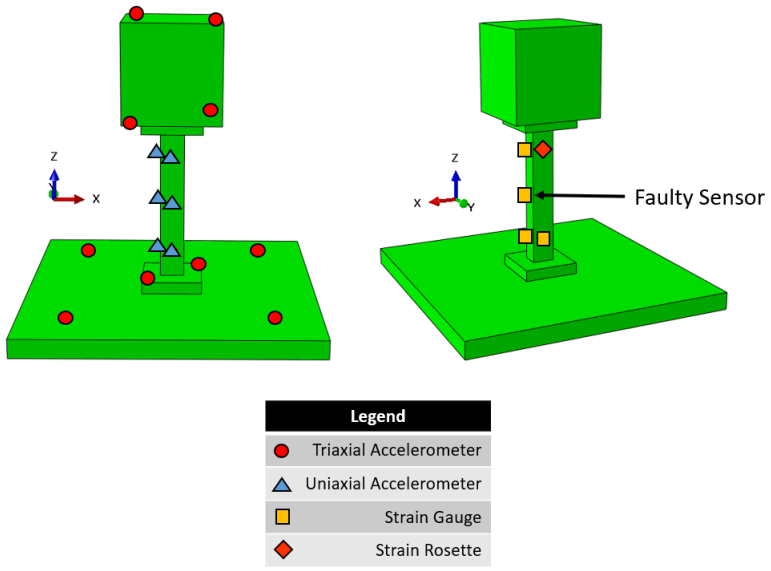

Figure 5: Accelerometer and strain gauge locations during physical testing.

When performing expansion about the entire structure, it was discovered that the twelve measured DOFs at the base had overall much lower accuracy than other locations. The DOFs used in the expansion are shown in Fig. 6. Section 6 studies the affect of including and excluding the twelve base DOFs.

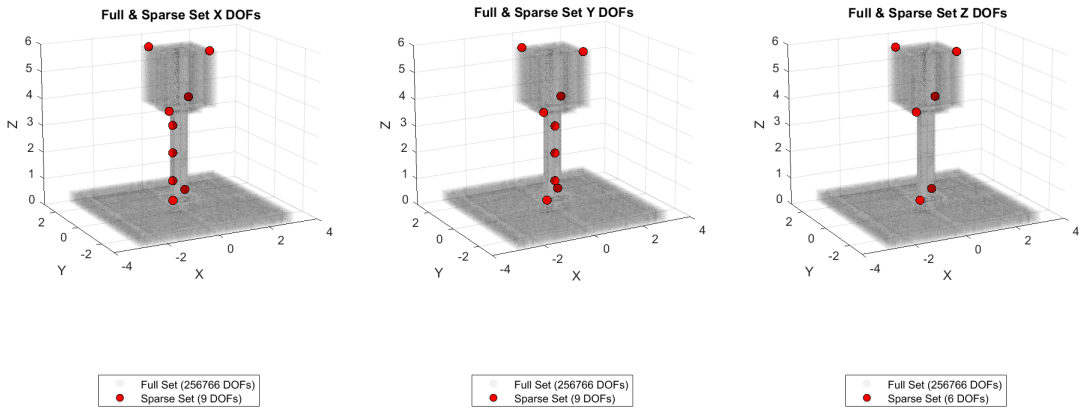

Figure 6: Sparse and full set of each independent direction used for SEREP.

5 Finite Element Model

A finite element model of the bobble head was created. The base, beam and block were modeled as nominal dimensions of the test hardware. Aluminum material properties were assigned to all components with a modulus of elasticity of $10(10^6)$ *psi* and a density of 0.098 $\frac{lb}{in^3}$. A continuous mesh was used, meaning that components were completely tied at contact surfaces. The bolts and sensors were not modeled. The lower surface of the base of the structure was constrained in all 6 DOFs as shown in

Fig. 7. The model consisted of 231,282 linear hexahedral elements and is shown in Fig. 8. A fine mesh on the beam was used to improve stress and strain computations of this component.

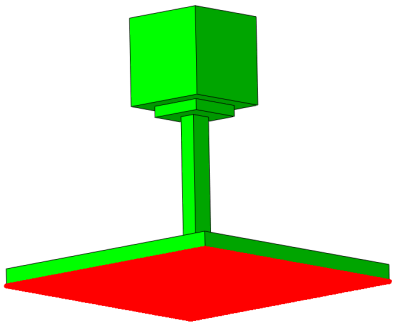

Figure 7: Finite element model boundary condition highlighted in red and constrained in 6 DOF.

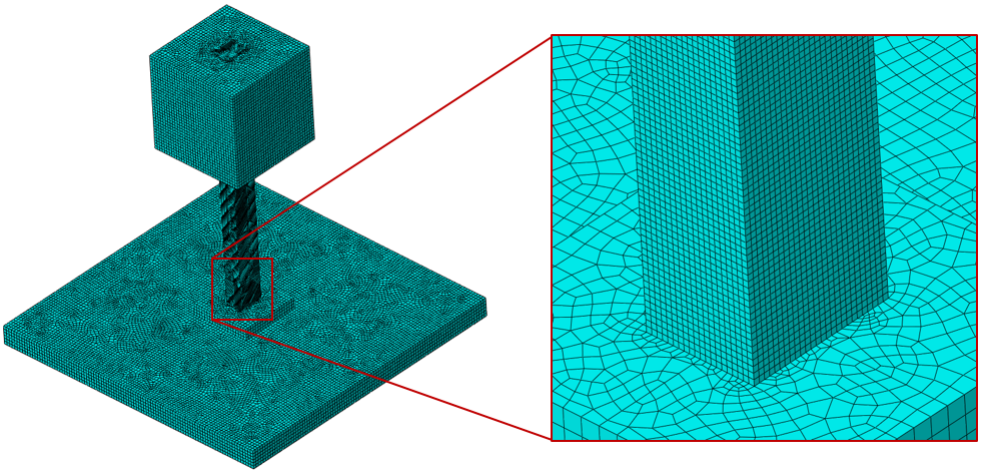

Figure 8: Geometry and mesh of finite element model.

A total of 12 modes were used for expansion including 6 rigid body and 6 flexible modes. These modes were selected because they align with the frequency band of the test. The test was controlled to a maximum frequency of 2 kHz and the frequency of the highest mode in the model was 2.46 kHz. The flexible displacement mode shapes and natural frequencies are shown in Appendix A.1, and the flexible strain mode shapes and natural frequencies are shown in Appendix A.2.

6 Verification

6.1 Modal Projection Error

The modal projection error was computed from Eq. 10 for two potential sparse data sets for expansion. It was computed from measured accelerometer data and the 12 finite element displacement mode shapes described in Section 5. The first set contained all accelerometer data from the test for a total of 36 responses. The second set contained all accelerometer data except for the twelve base DOFs associated with the base plate for a total of 24 responses. The DOFs for these sets are shown in Fig. 9. The modal projection error associated with each data set is shown in Fig. 10. The second data set with excluded base DOFs was used for strain estimation because it had lower average modal projection error. An explanation for the higher MPE in the first set is because the boundary condition assigned to the model over-constrains the base DOFs.

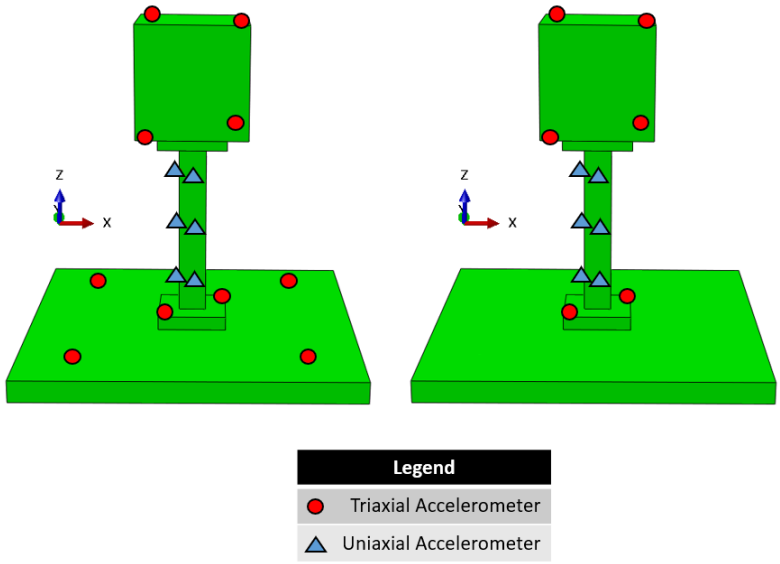

Figure 9: Degrees-of-freedom locations for MPE calculation when including (Left) and excluding (Right) the 12 base DOFs.

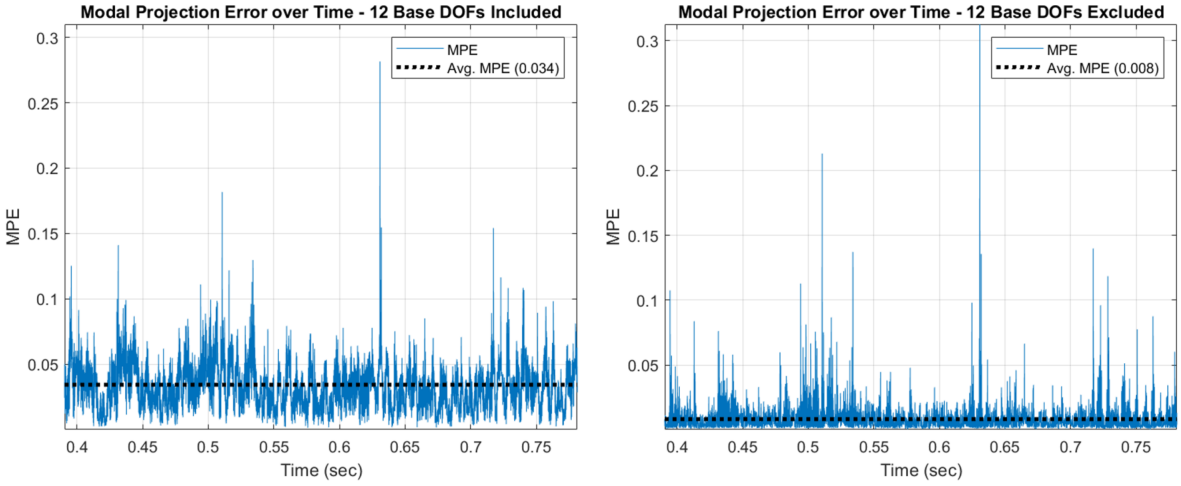

Figure 10: Modal projection error when including (Left) and excluding (Right) the 12 base DOFs.

6.2 Double Differentiation

The displacement estimation was verified by double differentiation as shown in Fig. 2. The method was verified in three directions and three locations, including the base of the beam, bottom of the bobble head and the top of the bobble head. The time history and PSD of the results are shown in Fig. 11 & 12 respectively. Note from the RMS values in Fig. 11 & 12 that the reconstructed accelerations underpredict the measured values. This may be due to the multiple filters applied to the data during integration. Figure 12 shows the in-band response from 50-2,000 Hz is reconstructed well.

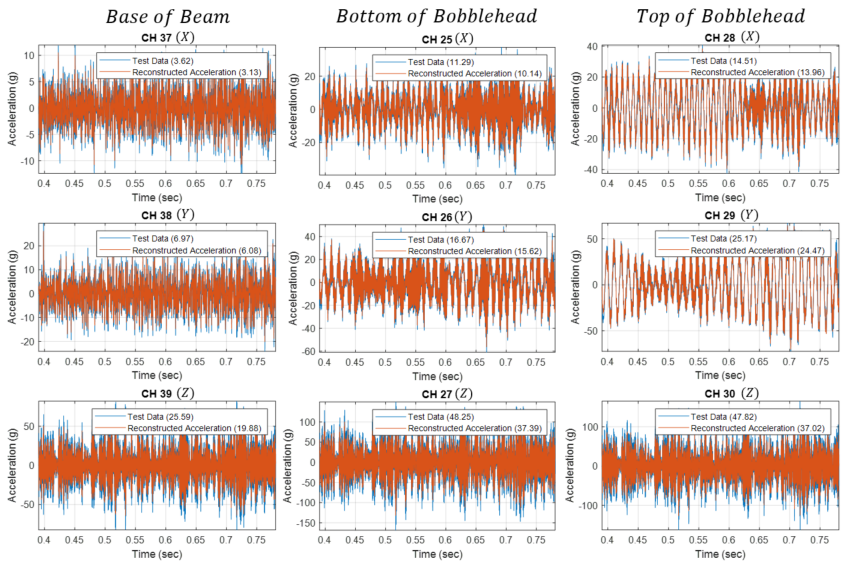

Figure 11: Acceleration time history data from physical measurement and reconstruction by double differentiation of estimated displacement. The RMS values are displayed in parentheses.

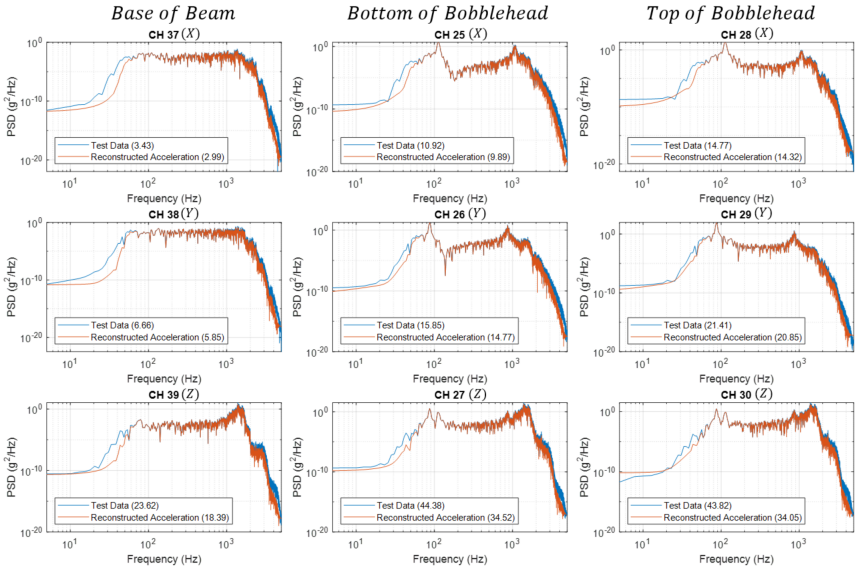

Figure 12: Acceleration power spectral density data from physical measurement and reconstruction by double differentiation of estimated displacement. The RMS values are displayed in parentheses.

7 Results

7.1 Acceleration Expansion

Acceleration expansion was performed prior to strain expansion to verify the expansion process. Acceleration was expanded over roughly a 0.4 second time interval. The measured and expanded acceleration data is overlaid in Fig. 13 at a single instance in time.

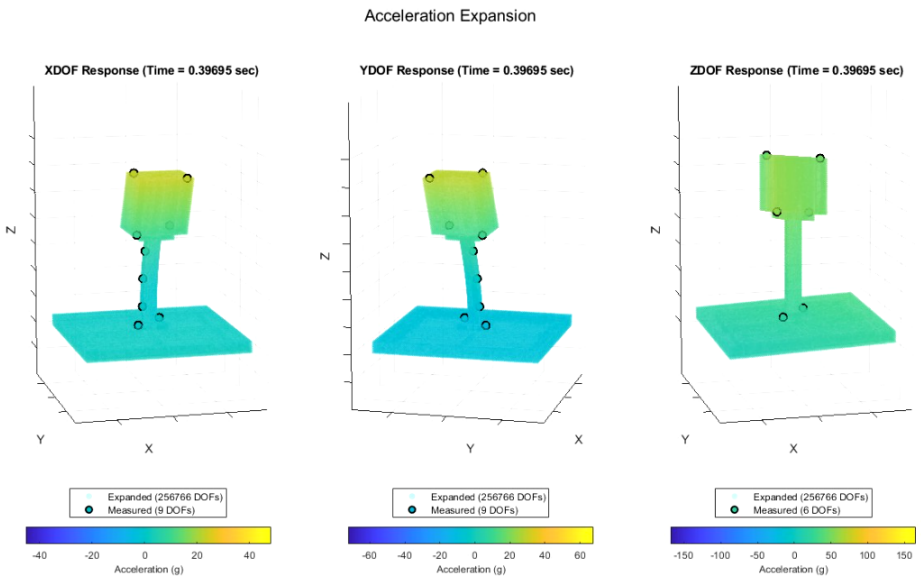

Figure 13: Measured and expanded acceleration data for each principal direction at a single instance in time.

The expanded accelerations are compared to measured accelerations by the methods listed in Section 2.5. Figure 14 compares RMS and MAE values in both the time and frequency domain. The MAE and values were generally low when compared to their respective RMS values, implying the acceleration expansion was accurate. Supplementary results are presented in Appendix A.4.

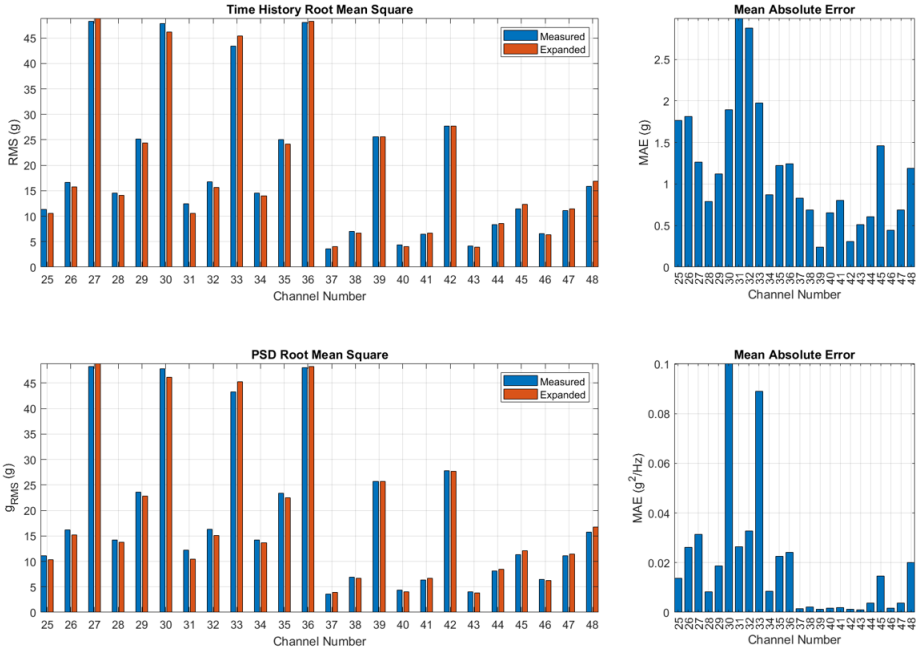

Figure 14: RMS (Left) and MAE (Right) for measured and expanded acceleration signals. The time and frequency domain metrics are displayed on the top and bottom respectively.

7.2 Strain Expansion

In this section, strain values from the estimation method are compared to measured values at four points on the structure. The locations, directions and sensor numbers are shown in Fig. 15. Note that all strains presented are in the Z direction per Fig. 15. The full estimated and sparse measured strains are shown at a single instance in time in Fig. 16.

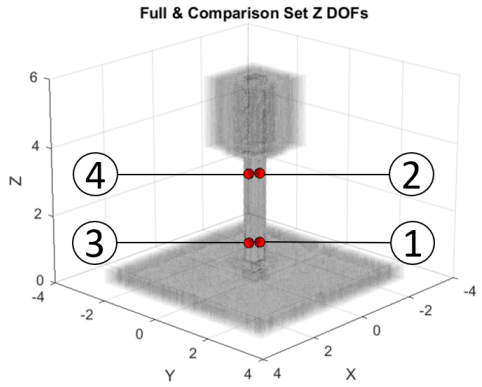

Figure 15: Strain locations marked as red dots with corresponding sensor numbers. The direction of strain is Z per the axis shown.

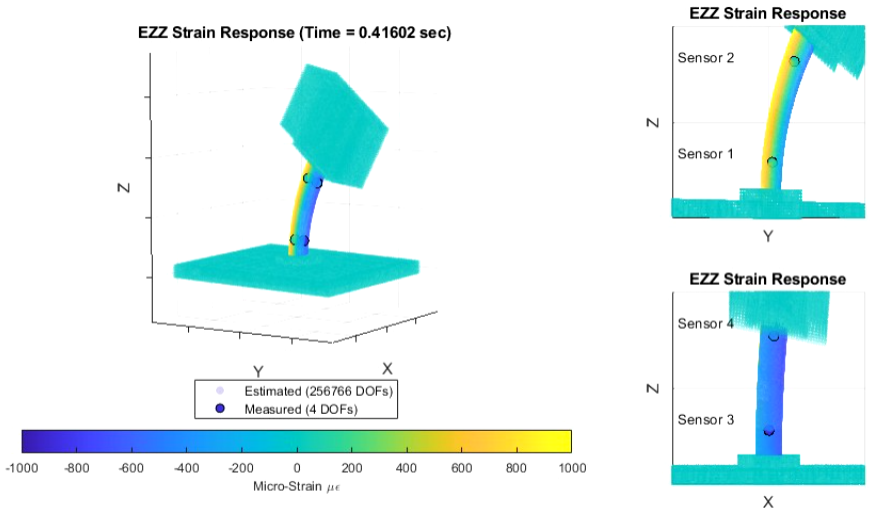

Figure 16: Measured and estimated strains in vertical direction (Z) at a single instance in time.

The strains are compared in the time domain in Fig. 17 and the frequency domain in Fig. 18. The error metrics, RMS and MAE, for the time and frequnecy domain are presented in Fig. 19. Upon inspection of Fig. 17-19, it can be noted that there is significant error between the estimated and measured strain values. Comparatively, the results from acceleration expansion per Section 7.1 had much lower error.

The frequency responses may be used to help characterize this error. Figure 18 shows two key characteristics of the strain responses. First, note that the peak in each signal around 100 Hz has a much greater amplitude than other peaks in the frequency range. Assuming the system response may be approximated by a linear combination of its natural frequencies and mode shapes, this indicates that the first few natural frequencies are the major contributors to the strain response. The strain mode shapes of the first two modes at 91 and 120 Hz are shown in Appendix A.2, Fig. 26-27. The second observation is that the majority of the error is concentrated at lower frequencies. Note that all sensors exhibit relatively lower error at frequencies above 1,000 Hz. In conclusion, there are significant errors in the strain estimate (Fig. 19), and the majority of these errors are

due to the lower frequency response (Fig. 18). Potential sources of this error are discussed in the following section.

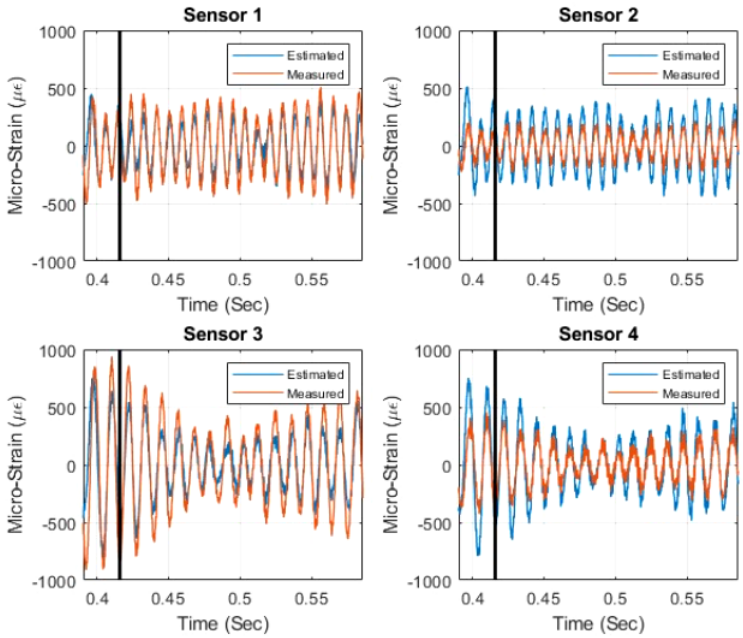

Figure 17: Strain time histories of measured and estimated strains per the corresponding sensor numbers defined in Fig. 15. The vertical black line represents the instance in time associated with Fig. 16.

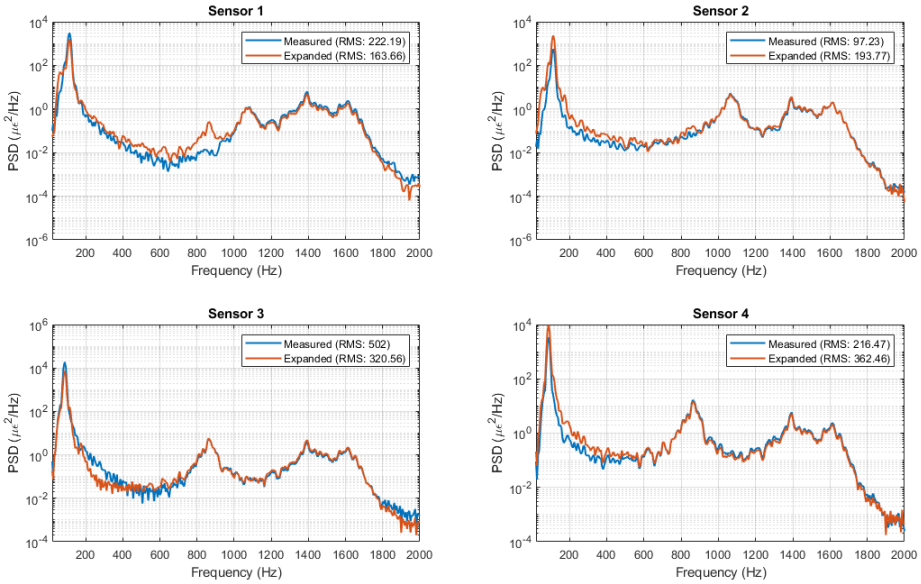

Figure 18: Strain power spectral densities of measured and estimated strains per the corresponding sensor numbers defined in Fig. 15.

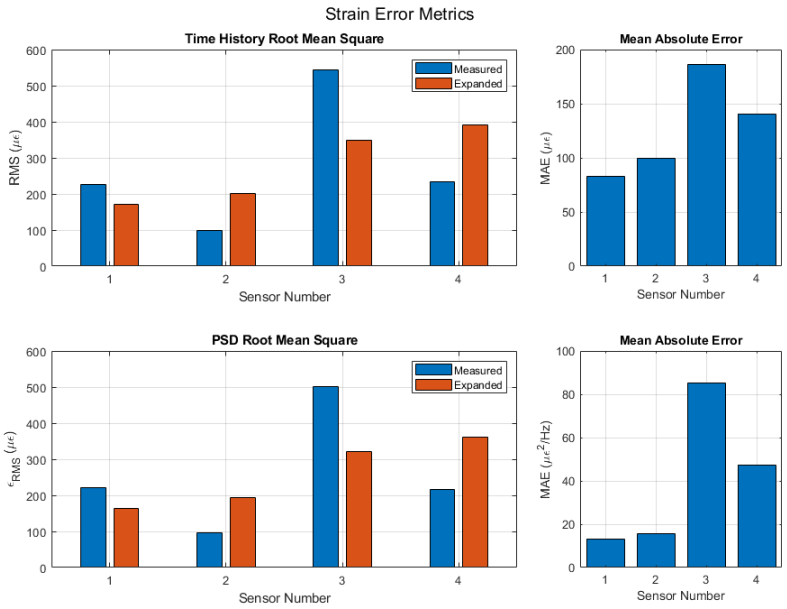

Figure 19: RMS (Left) and MAE (Right) of measured and estimated strains per the corresponding sensor numbers defined in Fig. 15.

8 Conclusion

Acceleration expansion and strain estimation were performed and evaluated on a physical test structure. Expansion of acceleration was shown to be accurate and enables assessment of the component's acceleration response at unmeasured locations. The strain estimation method produced significant error when compared to measured values. It can be concluded that accurate expansion of acceleration does not guarantee accurate estimation of strain when performing the proposed method.

Some anticipated sources of error are due to the following limitations. First, errors are introduced when estimating displacement from acceleration data. Other methods for estimating displacement from acceleration exist and could improve the strain estimate. Additionally, direct measurements of the displacement response would help validate displacement estimation techniques. Second, the uncalibrated mode shapes from the finite element model are another source of error. This error occurs because the physically measured values are fitted via the finite element mode shapes. Any discrepancies between experimental and model mode shapes will result in errors in this step. Further study of these limitations could improve the accuracy of strain estimation.

References

[1] J. O'Callahan, P. Avitabile, and R. Riemer. "System Equivalent Reduction Expansion Process (SEREP)". In: *Proceedings of the 7th International Modal Analysis Conference*. IMAC. 1989.

[2] B. Zwink et al. *Flight Environments Demonstrator: Part II - Ground Trials of a Sounding Rocket Experiment for Characterization of Flight*. Tech. rep. SAND2018-12092C. Sandia National Laboratories, Jan. 2019.

[3] J. Baqersad and K. Bharaqwaj. "Strain expansion-reduction approach". In: *Mechanical Systems and Signal Processing* 101 (2018), pp. 156–167.

[4] B. Witt, D. Rohe, and T. Schoenherr. *Full-Field Strain Shape Estimation From 3D SLDV*. Tech. rep. SAND2018-12119C. Sandia National Laboratories, 2018.

[5] Almarshad. *Building Drift Estimation Using Acceleration and Strain Measurements*. 2017.

[6] *How to 'correctly' integrate time data within Time Domain Integration?* SIEMENS^{TM}, 2016.

[7] T. Schoenherr, J. Rouse, and J. Harvie. *Characterizing dynamic test fixtures through the modal projection error*. Tech. rep. SAND2020-1119. Sandia National Laboratories, 2020.

[8] T. Schoenherr and J. Paripovic. "Using Modal Projection Error to Evaluate SEREP Modal Expansion". In: *Proceedings of the 38th International Modal Analysis Conference*. IMAC. 2021.

[9] T. Irvine. *Power Spectral Density Integration*. URL: `https://www.mathworks.com/matlabcentral/fileexchange/7600-power-spectral-density-integration`. (accessed: 10.06.2022).

[10] *FEMTools^{TM} Model Updating Theoretical Manual*. 2017.

A Appendices

A.1 Displacement Mode Shapes from Finite Element Model

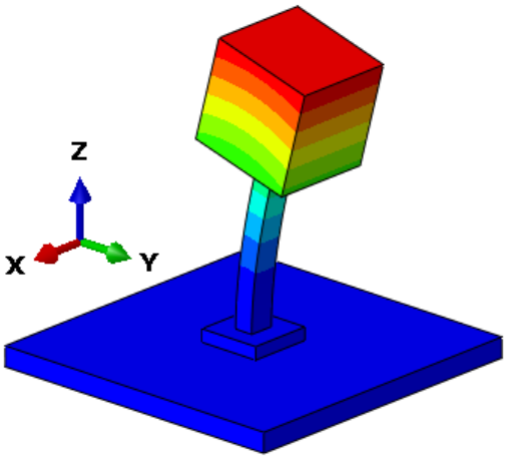

Figure 20: First flexible mode. First order bending in Y direction at 91 Hz.

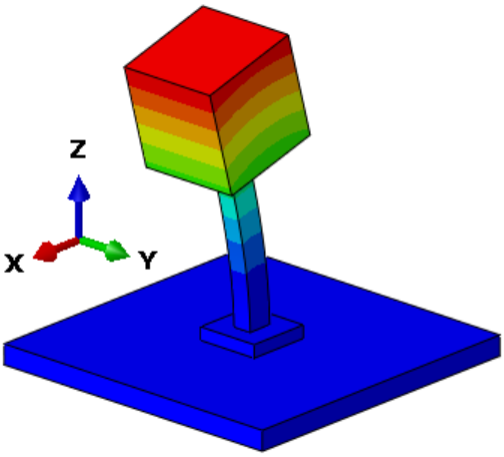

Figure 21: Second flexible mode. First order bending in X direction at 120 Hz.

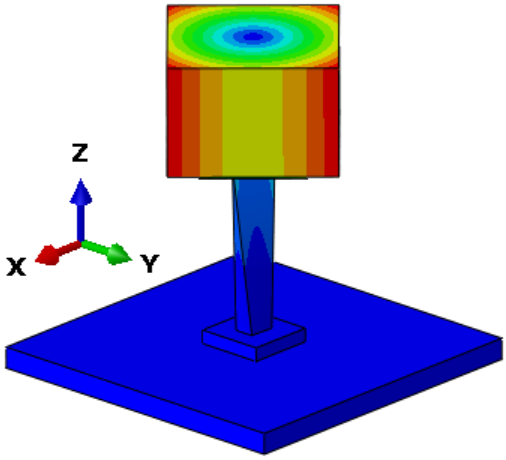

Figure 22: Third flexible mode. First order torsion in Z at 317 Hz.

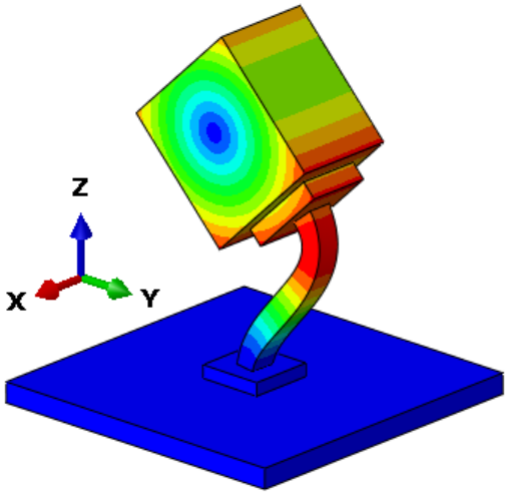

Figure 23: Fourth flexible mode. Second order bending in Y direction at 976 Hz.

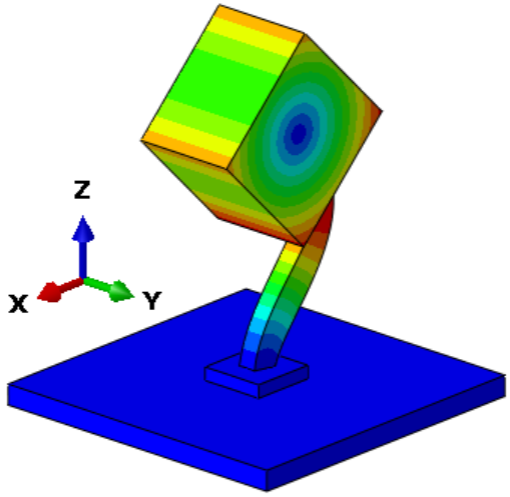

Figure 24: Fifth flexible mode. Second order bending in X direction at 1265 Hz.

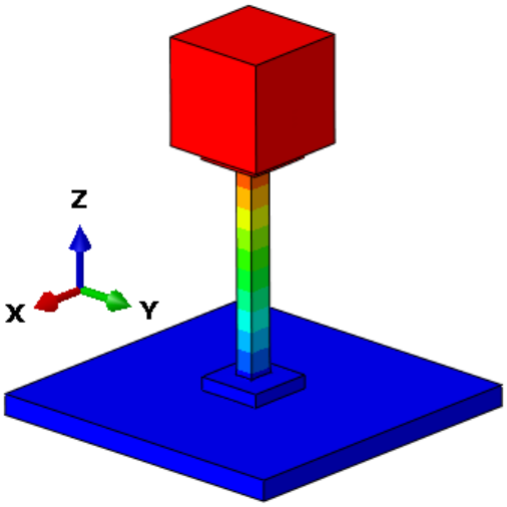

Figure 25: Sixth flexible mode. First order axial mode at 2462 Hz.

A.2 Strain Mode Shapes from Finite Element Model

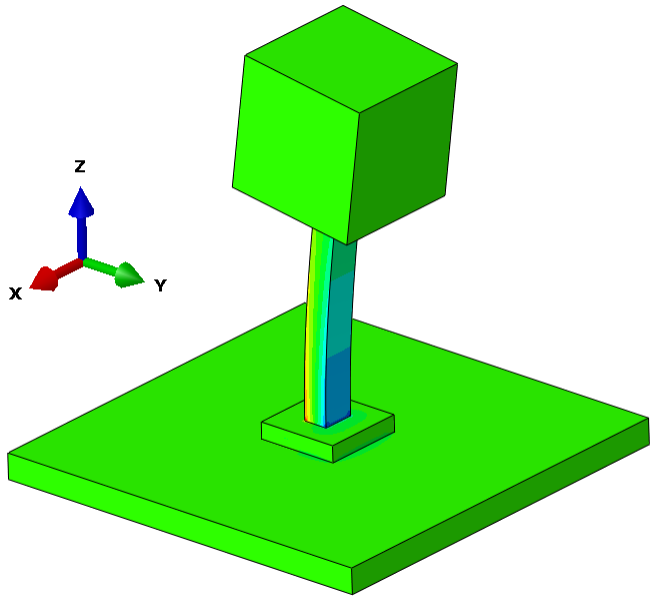

Figure 26: First flexible mode. First order bending in Y direction at 91 Hz.

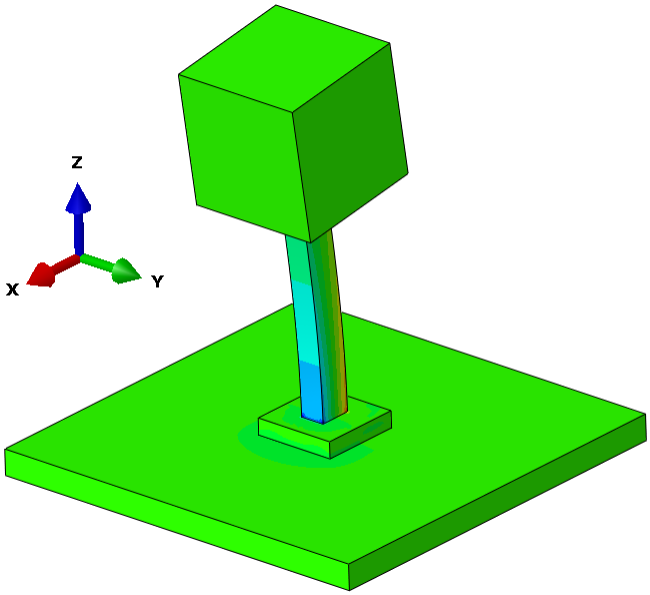

Figure 27: Second flexible mode. First order bending in X direction at 120 Hz.

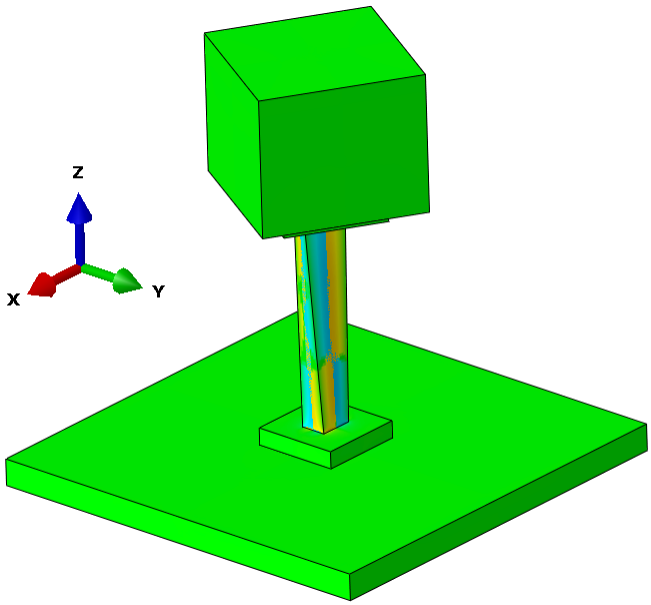

Figure 28: Third flexible mode. First order torsion in Z at 317 Hz.

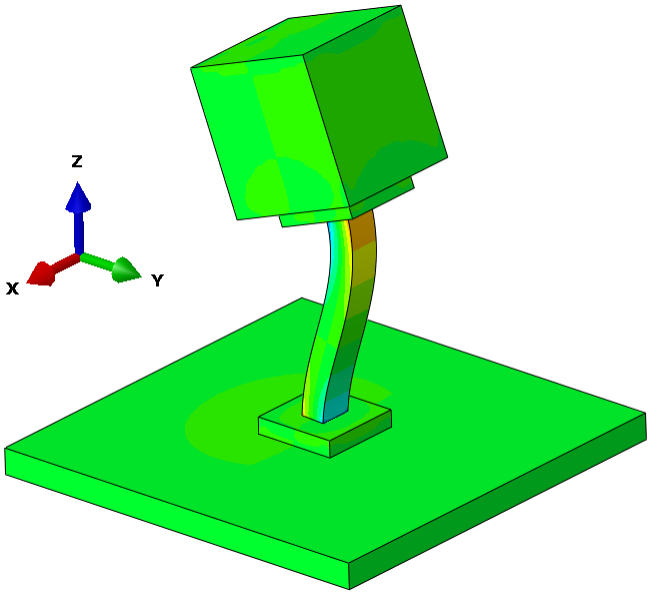

Figure 29: Fourth flexible mode. Second order bending in Y direction at 976 Hz.

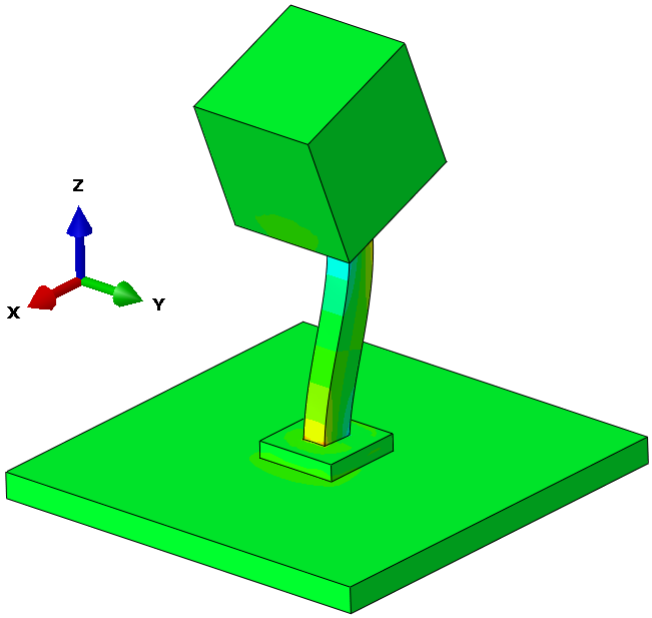

Figure 30: Fifth flexible mode. Second order bending in X direction at 1265 Hz.

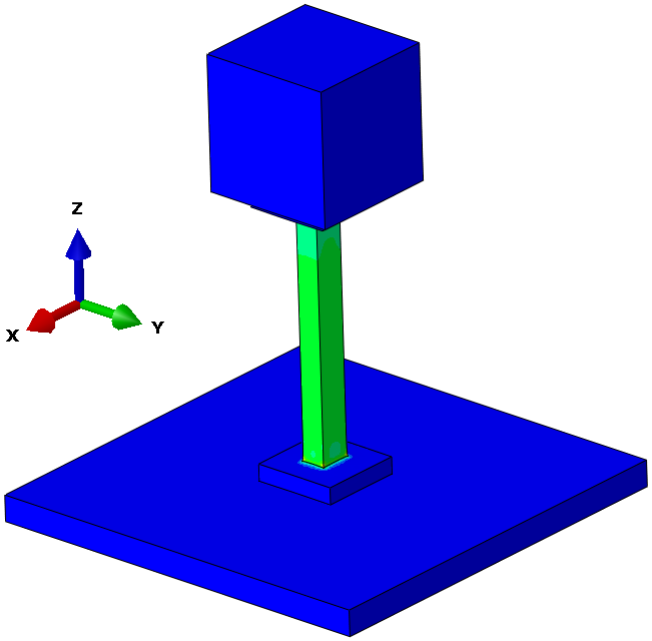

Figure 31: Sixth flexible mode. First order axial mode at 2462 Hz.

A.3 Supplementary Error Metrics

A.3.1 Time & Frequency Response Assurance Criterion

The time response assurance criterion (TRAC) and frequency response assurance criterion (FRAC) are both metrics that qualitatively compare two signals in the time and frequency domains respectively. The equation for TRAC is shown as Eq. 14 and the equation FRAC is shown as Eq. 15 per Dynamic Design Solutions [10]. A TRAC or FRAC of 1 indicates perfect

consistency and 0 indicates inconsistency or orthogonal signals.

$$TRAC = \frac{(|\overline{X}_{t,meas}{}^{\top}||\overline{X}_{t,pred}|)^2}{(|\overline{X}_{t,pred}{}^{\top}||\overline{X}_{t,meas}|)(|\overline{X}_{t,meas}{}^{\top}||\overline{X}_{t,pred}|)} \tag{14}$$

$$FRAC = \frac{(|\overline{X}_{f,meas}{}^{\top}||\overline{X}_{f,pred}|)^2}{(|\overline{X}_{f,pred}{}^{\top}||\overline{X}_{f,meas}|)(|\overline{X}_{f,meas}{}^{\top}||\overline{X}_{f,pred}|)} \tag{15}$$

A.3.2 Root Mean Squared Error

The root mean squared error (RMSE) compares two signals by computing the deviation between them. It may be computed in the time or frequency domain, as shown in Eq. 16 & 17 respectively. A low RMSE indicates good agreement between measured and predicted values.

$$RMSE_{time} = \sqrt{\frac{\sum_t (\overline{X}_{t,meas} - \overline{X}_{t,pred})^2}{n_t}} \tag{16}$$

$$RMSE_{freq} = \sqrt{\frac{\sum_f (\overline{X}_{f,meas} - \overline{X}_{f,pred})^2}{n_f}} \tag{17}$$

A.4 Supplementary Acceleration Expansion Results

The time and frequency domain responses of a few of the signals is studied in greater detail in Fig. 32 and 33 respectively. For succinctness, only three signals are shown. These signals were selected to represent a worst, average and best expansion of the total 24 signals based on the various error metrics discussed above. The TRAC and FRAC values are listed generally as SAC, which stands for Signature Assurance Criterion.

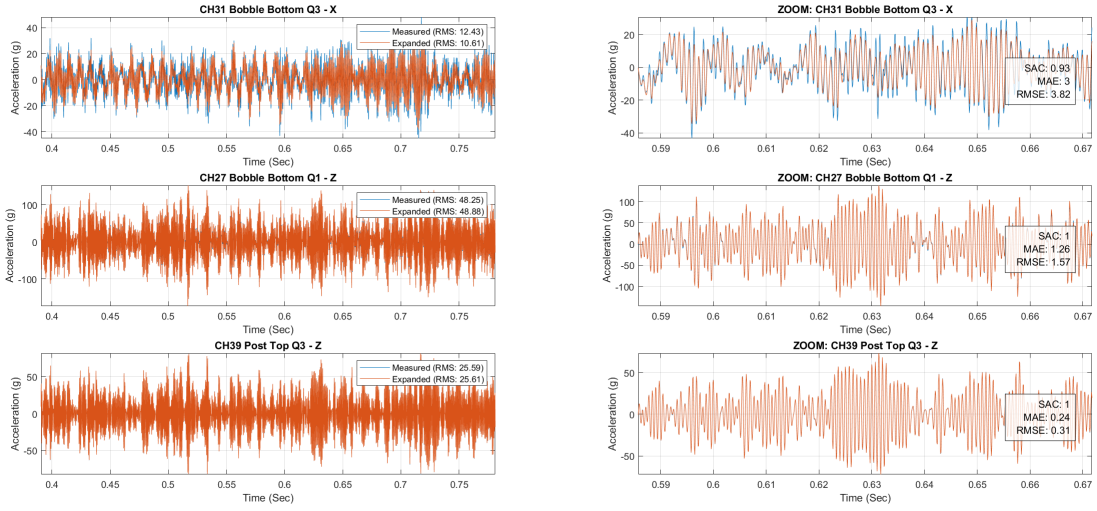

Figure 32: Acceleration time history compared between measured and expanded data of worst (Top), average (Middle) and best (Bottom) channels.

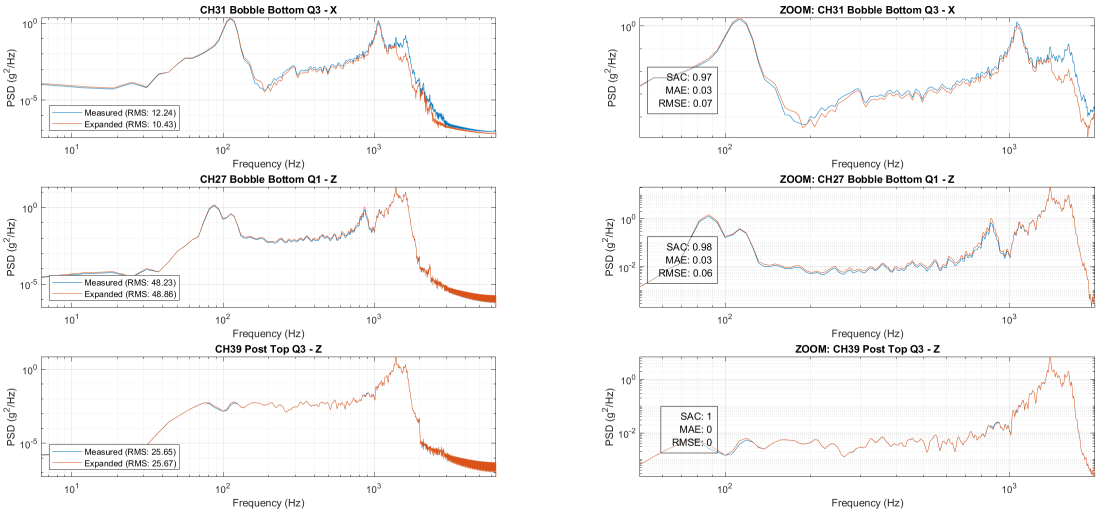

Figure 33: Acceleration power spectral density compared between measured and expanded data of worst (Top), average (Middle) and best (Bottom) channels.